Geophysical Research Letters

RESEARCH LETTER
10.1029/2021GL094185

Key Points:

- Brillouin spectroscopy and X-ray diffraction provide first constraints on the single-crystal elasticity of δ-(Al,Fe)OOH at mantle pressures
- Hydration decreases density but increases aggregate velocities of MORB in the shallow lower mantle
- Hydration of MORB increases the seismic velocity contrast with the background mantle

Supporting Information:

Supporting Information may be found in the online version of this article.

Correspondence to:

N. Satta,
niccolo.satta@earth.ox.ac.uk

Citation:

Satta, N., Criniti, G., Kurnosov, A., Boffa Ballaran, T., Ishii, T., & Marquardt, H. (2021). High-pressure elasticity of δ-(Al,Fe)OOH single crystals and seismic detectability of hydrous MORB in the shallow lower mantle. *Geophysical Research Letters*, *48*, e2021GL094185. https://doi.org/10.1029/2021GL094185

Received 10 MAY 2021
Accepted 8 NOV 2021

High-Pressure Elasticity of δ-(Al,Fe)OOH Single Crystals and Seismic Detectability of Hydrous MORB in the Shallow Lower Mantle

Niccolò Satta[1,2], Giacomo Criniti[1], Alexander Kurnosov[1], Tiziana Boffa Ballaran[1], Takayuki Ishii[1,3], and Hauke Marquardt[2]

[1]Bayerisches Geoinstitut, University of Bayreuth, Bayreuth, Germany, [2]Department of Earth Sciences, University of Oxford, Oxford, UK, [3]Center for High Pressure Science and Technology Advanced Research, Beijing, China

Abstract Oxyhydroxides like δ-(Al,Fe)OOH may stabilize "water" in Mid-Ocean Ridge Basalt (MORB) subducted into the Earth's lower mantle. The single-crystal elasticity of δ-(Al,Fe)OOH has not been experimentally constrained, hampering an accurate evaluation of the seismic detectability of this high-pressure solid solution, and the presence of "water," in the deep Earth. Here, we report the first experimental single-crystal elasticity results of δ-($Al_{0.97}Fe_{0.03}$)OOH measured by X-ray diffraction and Brillouin spectroscopy. We use our results to compute seismic properties of hydrous and anhydrous MORB at pressures and temperatures expected in slabs at shallow lower mantle conditions. We show that hydrous MORB is less dense than anhydrous MORB, but has faster aggregate seismic velocities. This suggests that hydration in MORB has an effect on velocities opposite to that observed in other lithologies, and further indicates that hydration of MORB increases the seismic contrast to the background mantle.

Plain Language Summary Water can be delivered into the Earth's mantle via subduction of hydrous phases, playing an active role in global-scale geological processes. Hence, tracking hydrous phases during subduction is pivotal to understand the geological evolution of our planet. At lower mantle depths, oxyhydroxides such as δ-(Al,Fe)OOH are the primary hosts of water in subducted oceanic crust. Here, we investigated the single-crystal elasticity of δ-($Al_{0.97}Fe_{0.03}$)OOH at pressures consistent with subduction in the upper mantle and transition zone. Our experimental results were used to evaluate the impact that hydration has on the physical properties of oceanic crust subducted into the lower mantle. For this purpose, we modeled density and aggregate properties of hydrous and anhydrous oceanic crust subducted into the lower mantle. Our modeling shows that hydration induces a reduction in the density of the modeled lithologies, but increases their aggregate velocities. Our results suggest that hydration may influence the subducting behavior of oceanic crust as well as their detectability through seismology.

1. Introduction

Constraining the hydration state of the Earth's mantle is crucial to model geodynamic processes and their control over lithospheric dynamics, as well as understanding processes that lead to planetary habitability (Ohtani, 2020). The transport of H_2O ("water") into the Earth's mantle is governed by the subduction of hydrated oceanic lithosphere (slabs) (Peacock, 1990). Thus, tracing the subduction of slabs and quantifying their water content with depth is of pivotal importance to constrain the influx of water into Earth's mantle.

Dense Hydrous Magnesium Silicates (DHMS), a group of hydrous phases likely present in cold subducting slabs, are expected to retain water down to the deepest regions of the Earth's mantle (Ohira et al., 2014). Phase relations experiments report DHMS to form within the harzburgitic layer of subducting slabs (Frost, 1999; Ohtani et al., 2001, 2004), and the upper sediment layer (Ono, 1998). The oceanic crust, Mid-Ocean Ridge Basalt (MORB), localized between the harzburgitic and sediment layers, has historically been regarded as a poor host for water (Ono, 1998). However, it has been recently shown that solid solutions between the oxyhydroxides phase H ($MgSiO_4H_2$), δ-AlOOH and ε-FeOOH can form within hydrous oceanic crust at shallow lower mantle pressures (Liu et al., 2019). This finding indicates that MORB may play a pivotal role in the global deep water cycle, and highlights the importance of members of the H-δ-ε solid solution as the most likely hosts of water within cold oceanic crust entering the lower mantle.

Previously, δ-AlOOH and ε-FeOOH have been investigated by both theoretical and experimental studies documenting a wide pressure (P)-temperature (T) stability field that stretches up to the core-mantle boundary (Hsieh et al., 2020; Lu & Chen, 2018; Mashino et al., 2016; Nishi et al., 2015, 2019; Ohira et al., 2019; Sano et al., 2004; Sano-Furukawa et al., 2008, 2018; Simonova et al., 2020; Su et al., 2020; Thompson et al., 2017, 2020; Xu et al., 2019). The single-crystal elastic properties of these oxyhydroxides have only been previously described by theoretical studies, with no experimental confirmation.

At ambient conditions, the crystal structure of δ-AlOOH and ε-FeOOH (Figure S1a in Supporting Information S1) has space group $P2_1nm$ and consists of edge-sharing (Al,Fe)O_6 octahedral chains parallel to the c-axis, connected with each other through vertices (Gleason et al., 2008; Komatsu et al., 2006). A structural phase transition in δ-AlOOH and δ-(Al,Fe)OOH occurs at about 8–10 GPa, inducing an increase in symmetry from $P2_1nm$ to $Pnnm$ (Ohira et al., 2019; Sano-Furukawa et al., 2018). This transition causes clear changes in the axial compressibility (Kuribayashi et al., 2014; Sano-Furukawa et al., 2009, 2018). Similar changes in the axial compressibility have been observed in ε-FeOOH at about 18 GPa, suggesting that Fe substitution increases the transition pressure of the $P2_1nm$ to $Pnnm$ phase transition (Thompson et al., 2020). The $Pnnm$ structure of δ-AlOOH displays a disordered configuration of the hydrogen (H) bonds (Figure S1b and S1c in Supporting Information S1) at the onset of the $P2_1nm$ to $Pnnm$ phase transition. The H bond symmetrization is completed between 16 and 18.1 GPa (Sano-Furukawa et al., 2018). Therefore, the δ-AlOOH-rich solid solutions have $Pnnm$ space group and symmetric H bonds in the lower mantle.

Here, we performed simultaneous X-ray diffraction (XRD) and Brillouin spectroscopy experiments on δ-$(Al_{0.97}Fe_{0.03})$OOH single crystals up to 17.09(5) GPa to constrain the full elastic tensor of the $Pnnm$ phase, that is, the stable phase at lower mantle conditions. XRD experiments were carried out up to 19.98(3) GPa. Our results were used, together with those available in the literature, to calculate aggregate properties of hydrous and anhydrous MORB in a P-T window relevant for slabs stagnating in the shallow lower mantle. Our model shows that despite being less dense, hydrous MORB is characterized by faster aggregate velocities with respect to anhydrous MORB, increasing the seismic velocity contrast to the background mantle.

2. Materials and Methods

2.1. Material Synthesis and Characterization

Single crystals of δ-(Al,Fe)OOH were synthesized in a multi-anvil apparatus at the Bayerisches Geoinstitut (BGI), University of Bayreuth, following the procedure described by Kawazoe et al. (2017). Two crystals, hereafter named H4765x1 and H4765x2, were selected based on their quality. These crystals have $P2_1nm$ space group at room conditions as determined by the presence of the $h + l = 2n + 1$ for $k0l$ and $k + l = 2n + 1$ for $0kl$ reflections. H4765x1 and H4765x2 crystals were oriented parallel to the (142) and (201) planes, and double-sided polished to a final thickness of about 15 μm. The oriented platelets were cut into half-circles for high-pressure experiments using a Focused Ion Beam (FIB) (Figure S2 in Supporting Information S1) (Marquardt & Marquardt, 2012; Schulze et al., 2017). After FIB cutting, the final orientations in Cartesian coordinates ($e_2 \| b$, $e_3 \| c$) are (0.103, 0.836, 0.539) and (0.784, 0.021, 0.620) for H4765x1 and H4765x2, respectively. Further details on the synthesis procedure, quality assessment, sample selection, and FIB cutting can be found in Text S1 in Supporting Information S1.

The chemical compositions of the H4765x1 and H4765x2 were measured on half-circles, one from each of the two platelets, using an Electron Microprobe. Mössbauer spectroscopy was used to determine their Fe^{3+}/Fe_{tot} ratio (Text S2 in Supporting Information S1). According to our results, the chemical formula normalized to two oxygens per formula unit is $Al_{0.972(7)}Fe^{3+}_{0.028(1)}OOH$ for H4765x1, and $Al_{0.977(9)}Fe^{3+}_{0.023(1)}OOH$ for H4765x2.

2.2. High-Pressure Experiments

High-pressure measurements were carried out in a BX90 diamond-anvil cell (DAC) (Kantor et al., 2012), equipped with diamonds having a culet size of 400 μm. A laser-drilled 250 μm diameter hole was used as pressure chamber in a pre-indented Re gasket. Two FIB-cut platelets were loaded in the pressure chamber together with a ruby sphere used for pressure determination (Dewaele et al., 2004). High-pressure data were collected during

three distinct runs, in which either He or Ne was used as pressure transmitting medium (Text S3 in Supporting Information S1).

Simultaneous XRD and Brillouin spectroscopy experiments on the *Pnnm* phase of δ-($Al_{0.97}Fe_{0.03}$)OOH were performed between 8.67(1) and 17.09(5) GPa at the BGI. Further XRD experiments were performed up to 19.98(3) GPa. Technical details of the instrument installed at BGI are reported in Text S4 in Supporting Information S1 and elsewhere (Trots et al., 2011, 2013). In our XRD investigations, no reflections relative to the $P2_1nm$ space group have been detected (Text S5 in Supporting Information S1), confirming that the $P2_1nm$ to *Pnnm* phase transformation had occurred before 8.67(1) GPa.

Brillouin spectroscopy experiments were performed at six distinct pressure points, for each platelet at different rotation angle (χ) with 20° interval over a 360° angular range. Details on the data analysis are provided in Text S4 in Supporting Information S1. The *Pnnm* phase of δ-(Al,Fe)OOH has orthorhombic symmetry, hence its elastic stiffness tensor consists of nine independent, non-zero coefficients (c_{ij}) that in Voigt notation are (Nye, 1985): c_{11}, c_{22}, c_{33}, c_{44}, c_{55}, c_{66}, c_{12}, c_{13}, c_{23}. All nine c_{ij} were constrained at each pressure point (Table S3 in Supporting Information S1) by fitting the χ-dependent variation of the acoustic compressional velocity, v_P, and the two shear wave velocities, v_{S1} and v_{S2}, for both H4765x1 and H4765x2 platelets in a least-square fitting procedure of the Christoffel equation (Haussühl, 2007):

$$\left| c_{ijkl} n_j n_l - \rho v^2 \delta_{ik} \right| = 0 \quad (1)$$

where c_{ijkl} are the elastic stiffness coefficients in tensorial notation, $n_j n_l$ the phonon direction cosines, ρ the density calculated from the unit-cell volumes obtained by XRD (Text S4 in Supporting Information S1), and δ_{ik} the Kronecker delta. Voigt and Reuss bounds of the adiabatic bulk (K_S) and shear moduli (G) were calculated using the c_{ij} and elastic compliance coefficients, s_{ij}, respectively.

3. Results and Discussion

3.1. High-Pressure Elasticity of δ-(Al,Fe)OOH

Unit-cell volumes of H4765x1 and H4765x2 of the *Pnnm* phase (Table S1 in Supporting Information S1) have been normalized with respect to their values measured at 8.67(1) GPa and fitted using a third-order Birch-Murnaghan equation of state (BM3) (Birch, 1947) implemented in the EoSFit7 software (Angel et al., 2014; Gonzalez-Platas et al., 2016) using 8.67 GPa as reference pressure. The room pressure volume (V_0), isothermal bulk modulus (K_{T0}) and its corresponding first pressure derivative (K'_{T0}) were then calculated by extrapolation to ambient pressure. Results are reported in Table S2 in Supporting Information S1, while volumes normalized with respect to the Equation of State (EoS) parameter V_0 are plotted in Figure 1a together with literature data. The difference between this and previous studies (Figure 1a, Table S2 in Supporting Information S1) results from a trade-off in the V_0, K_{T0}, and K'_{T0} fitting parameters which complicate a quantitative assessment of the effect of Fe substitution on the compressibility of δ-AlOOH. The *Pnnm* ε-FeOOOH end-member is more compressible than δ-AlOOH (Thompson et al., 2020). However, the K_{T0} values obtained using a second-order Birch-Murnaghan equation of state (BM2), with K'_{T0} fixed to the value of 4 (Sano-Furukawa et al., 2009; Su et al., 2020; Table S2 in Supporting Information S1) show that samples with 5% of FeOOH substitution have the same K_{T0} as δ-AlOOH. The very low K_{T0} values reported by Ohira et al. (2019) are due to the relatively large K'_{T0} which are, however, poorly constrained. Due to the high quality of our data, we were able to tightly constrain the value of K'_{T0} which is clearly larger than 4. As a consequence, the value of K_{T0} appears slightly smaller than those reported for δ-AlOOH and δ-($Al_{0.956}Fe_{0.044}$)OOH (Table S2 in Supporting Information S1). A K_T-K'_{T0} confidence ellipse is provided in Figure S4 in Supporting Information S1.

The linear moduli, k, their first pressure derivatives, k', and the unit-cell parameters at ambient conditions (a_0, b_0, and c_0) have been obtained by fitting of a linearized BM3 implemented in EosFit7 (Angel et al., 2014), following the same procedure described for the unit-cell volumes. Results are tabulated in Table S2 in Supporting Information S1, and unit-cell parameters normalized to their EoS room pressure values are plotted versus pressure in Figure S5 in Supporting Information S1. No anomalies in the axial compressibility or the unit-cell axial ratios a/b, b/c, and a/c (Figure S6 in Supporting Information S1) have been observed up to the highest pressure point, that is, 19.98(3) GPa.

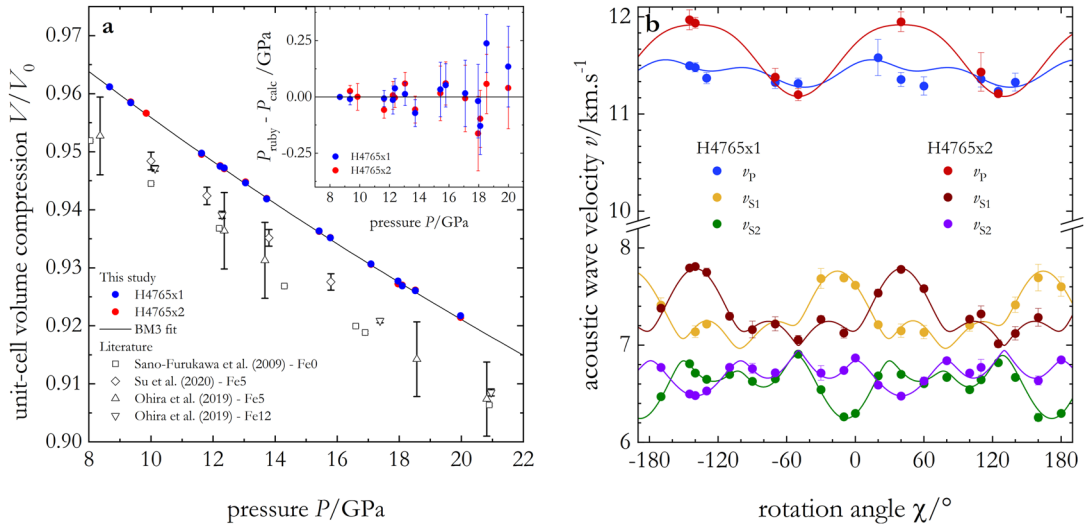

Figure 1. High-pressure experimental results on the *Pnnm* phase of δ-(Al,Fe)OOH. (a) Unit-cell volumes of *Pnnm* δ-$(Al_{0.97}Fe_{0.03})$OOH normalized with respect to the room pressure EoS parameter V_0 as function of pressure (filled circles) compared with literature data on *Pnnm* δ-(Al,Fe)OOH (open symbols). Solid curve: BM3 fit to the measured data; the inset plot shows the differences between ruby pressure, P_{ruby} (Table S1 in Supporting Information S1), and pressures calculated using the BM3 EoS parameters (P_{calc}, Table S2 in Supporting Information S1) as function of P_{ruby}. Differences are well within uncertainties, with an average deviation of 0.08 GPa and maximum deviation of 0.2 GPa (about 1%). (b) Observed (filled symbols) and calculated (solid curves) acoustic wave velocities of both single-crystals platelets of δ-$(Al_{0.97}Fe_{0.03})$OOH as a function of the rotation angle χ at 17.09(5) GPa.

Measured and calculated acoustic wave velocities obtained for both platelets at a pressure of 17.09(5) GPa are shown in Figure 1b, while a representative Brillouin spectrum is reported in Figure S7 in Supporting Information S1. The c_{ij} and density values for each individual pressure are summarized in Table S3 and Figure S8 in Supporting Information S1. All c_{ij} smoothly increase across the investigated pressure range, and their high-pressure behavior can be described by third-order finite strain expressions reported for individual c_{ij} (Stixrude & Lithgow-Bertelloni, 2005; Text S6 in Supporting Information S1).

Ab initio Density Functional Theory (DFT) calculations have reported discrepant results on the c_{ij} behavior of δ-AlOOH at high pressures (Cortona, 2017; Pillai et al., 2018; Tsuchiya & Tsuchiya, 2009). Our results are plotted together with Cortona (2017) and Tsuchiya and Tsuchiya (2009) in Figure S8 in Supporting Information S1. There is a very good agreement between our measured c_{22}, c_{44}, c_{55}, c_{66}, and c_{13} values and those reported in the literature, whereas the other experimental c_{ij} exhibit a different evolution with pressure (Figure S8 in Supporting Information S1). However, discrepancies are negligible for the aggregate elastic moduli (Figure 2a, the next section).

3.2. Aggregate Properties of δ-(Al,Fe)OOH

Voigt and Reuss bounds of the adiabatic bulk modulus K_S and shear modulus G were calculated at each pressure using the c_{ij} constrained in this study (Nye, 1985). Reuss-Voigt-Hill averages of K_S and G were calculated as the arithmetic mean between Reuss and Voigt values (Hill, 1952; Table S4 in Supporting Information S1). Both K_S and G show a monotonic increase with absolute pressure (Text S7 in Supporting Information S1) that can be described with third-order Eulerian finite strain equations (Stixrude & Lithgow-Bertelloni, 2005), as shown in Figure 2a. Fit results are reported in Table S5 in Supporting Information S1. To facilitate comparison, we used the same approach to fit theoretical data (Cortona, 2017) between 10 and 30 GPa (Figure 2a). Moreover, our K_S and G values show negligible differences with the theoretical prediction from Cortona (2017).

The aggregate compressional, v_P, and shear, v_S wave velocities (Text S4 in Supporting Information S1) of the sample investigated in this study are slightly faster than those reported by previous Brillouin spectroscopy results on powdered samples of δ-AlOOH (Mashino et al., 2016) and δ-$(Al_{0.956}Fe_{0.044})$OOH (Su et al., 2020; Figure 2b). The discrepancies between our results and those available in the literature cannot be simply explained by compositional differences since the small amount of Fe^{3+} present in our samples and in that of Su et al. (2020) should have a limited effect on the wave velocity of *Pnnm* phase of δ-AlOOH as it has no detectable effect on

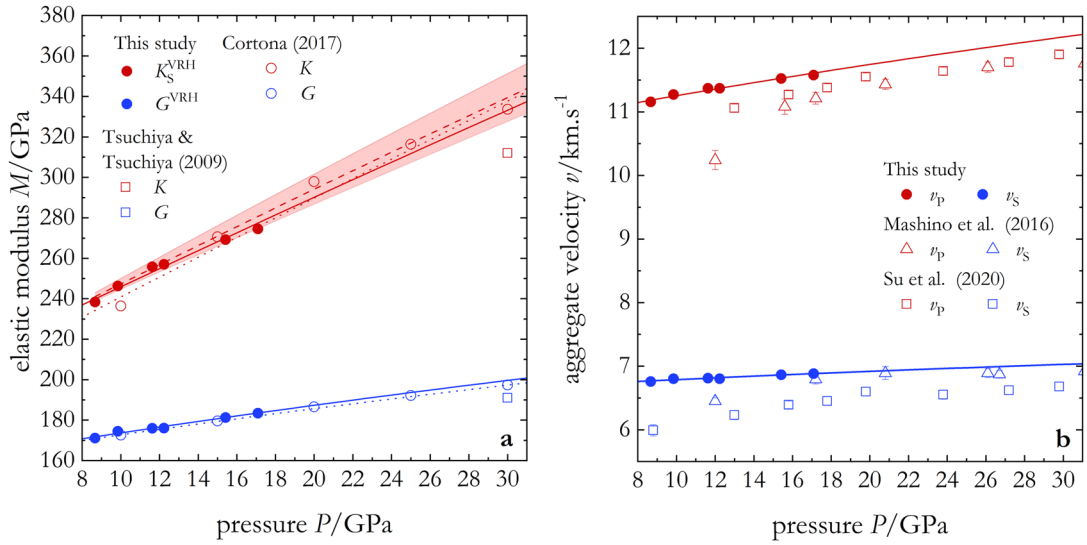

Figure 2. Voigt-Reuss-Hill averages of (a) Aggregate elastic moduli and (b) Velocities of δ-$(Al_{0.97}Fe_{0.03})OOH$ as a function of pressure. Closed and open symbols are our and literature data, respectively. The solid lines are fits to adiabatic aggregate moduli and aggregate velocity. The dashed line in panel (a) shows the calculated K_T based on our XRD results with uncertainties represented by the red shading. Dotted lines are fits to Cortona's (2017) data. All fits are based on 3rd-order Eulerian finite strain equations (Stixrude & Lithgow-Bertelloni, 2005). Most uncertainties are within the symbol size.

its compressibility (Table S2 in Supporting Information S1). However, Brillouin spectroscopy experiments on powdered samples can be affected by crystallographic preferred orientation, grain-grain interactions, and/or opto-elastic coupling effects that can influence wave velocities (Marquardt & Thomson, 2020) and may explain the observed discrepancies. The acoustic wave velocities measured for ε-FeOOH up to 24 GPa (Ikeda et al., 2019) are much slower than those reported here. However, they cannot be used to assess quantitively the effect of Fe substitution as ε-FeOOH has the $P2_1nm$ space group below about 17 GPa (Thompson et al., 2020).

3.3. Implications for the Detection of Water in Stagnant Slabs in the Shallow Lower Mantle

The interpretation of seismological observations is crucial to track the transport of hydrous material in subduction zones (Wang et al., 2020), including that associated with the subduction of hydrous MORB (e.g., Garth & Rietbrock, 2014, 2017). Seismic tomography indicates that subducting slabs enter the lower mantle in several locations, and sometimes stagnate at the top of the lower mantle (e.g., Fukao & Obayashi, 2013). Analysis of diamond inclusions further suggests that oceanic crust is recycled into the lower mantle (Nestola et al., 2018), where it might explain low-velocity seismic wave observations detected at the top of the lower mantle (Gréaux et al., 2019).

Recent phase relation experiments have shown that hydrous MORB is capable of retaining water down to the lower mantle through a continuous chain of stable hydrous phases, ending with the solid solution formed by phase H ($MgSiO_4H_2$), δ-AlOOH, and ε-FeOOH (H-δ-ε) at pressures exceeding 25 GPa (Liu et al., 2019). Here, we combine our single-crystal elasticity data set on δ-$(Al_{0.97}Fe_{0.03})OOH$ with previous results (Table S6 in Supporting Information S1) to compute the aggregate properties of hydrous and anhydrous MORB in a *P-T* window relevant for slabs in the shallow lower mantle. Our model is based on the thermodynamic formalism of Stixrude and Lithgow-Bertelloni (2005), and relies on mineral volume fractions and compositions constrained by previous experimental studies at relevant *P-T* conditions (Ishii et al., 2019; Liu et al., 2019; Tables S7 and S8 in Supporting Information S1). The aggregate elastic moduli and density of the *Pnnm* phase of δ-$(Al_{0.97}Fe_{0.03})OOH$ have been extrapolated to 30 GPa. This is justified by the fact that previous XRD results (e.g., Sano-Furukawa et al., 2009) show a smooth and continuous behavior of the unit-cell volume compression for *Pnnm* δ-AlOOH up to pressures above 30 GPa, suggesting that the H bond symmetrization does not cause any detectable discontinuity in the elastic behavior of these H-δ-ε oxyhydroxides. In our model, H-δ-ε oxyhydroxide in hydrous MORB is treated as a two-component mixture with molar ratio of $MgSiO_4H_2$:$(Al_{0.97}Fe_{0.03})OOH$ = 25:75. The small Fe content is consistent with the recent phase relations reported for hydrous MORB (Liu et al., 2019). The bulk modulus

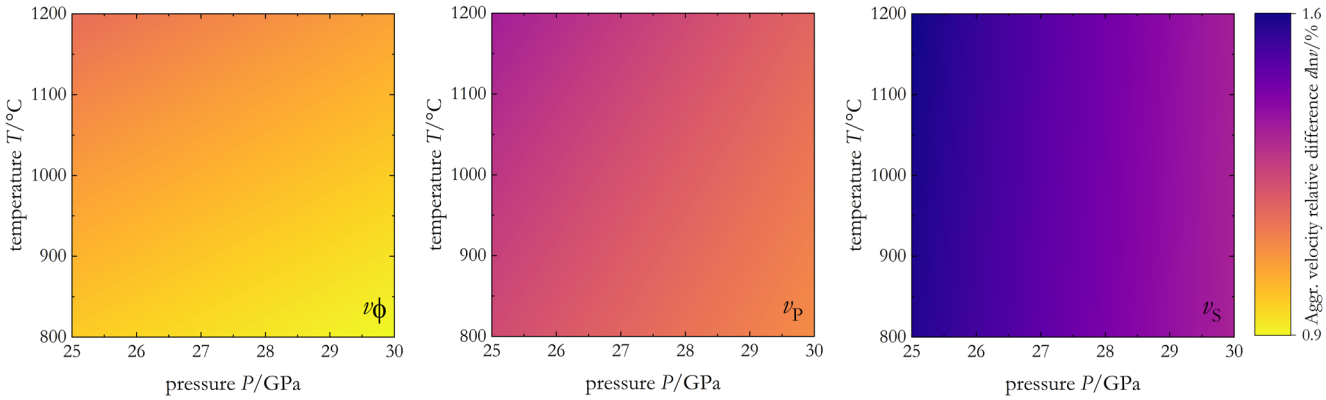

Figure 3. Relative differences between hydrous and anhydrous MORB in terms of aggregate velocities v_ϕ, v_P, and v_S (from the left to the right) across a *P-T* window relevant for slabs in the shallow lower mantle. Color scale applies to all three plots.

used for the modeling of phase H is determined from the *P-V-T* data reported by Nishi et al. (2018) data, while our single-crystal elasticity data set is used to model δ-$(Al_{0.97}Fe_{0.03})OOH$. Since no experimental constraints on the shear modulus at ambient pressure or its pressure derivative is currently available for phase H, they are assumed identical to those of δ-$(Al_{0.97}Fe_{0.03})OOH$. Moreover, the thermal parameters of δ-$(Al_{0.97}Fe_{0.03})OOH$ are assumed identical to those of δ-AlOOH (Duan et al., 2018), while those of phase H are determined by refitting the *P-V-T* data of Nishi et al. (2018) using a Debye model (Stixrude & Lithgow-Bertelloni, 2005). Our model does not solely consider the formation of H-δ-ε oxyhydroxides as a distinctive feature of MORB hydration, but it also takes into account various factors including the reduction of SiO_2 stishovite content and a depletion of its Al concentration, as well as the complete dissolution of minerals such as calcium ferrite and (Mg,Fe)O—all based on the latest phase relation results used as references for our modeling (Ishii et al., 2019; Liu et al., 2019). Isotropic aggregate properties were calculated between 25 and 30 GPa, corresponding to depths of 700–800 km, and at temperatures of 800°C–1200°C, covering the *P-T* range expected in subducting slabs entering the lower mantle (Kirby et al., 1996). Further details of the modeling are included in Text S8 in Supporting Information S1.

Our model indicates that densities of hydrous MORB are reduced by 2.5% with respect to anhydrous MORB. However, the hydration of MORB through the formation of H-δ-ε oxyhydroxides results in an increase of all the aggregate velocities, v_S, v_P, and v_ϕ, of up to 1.6% for v_S (Figure 3). Noticeably, MORB hydration through the formation of H-δ-ε oxyhydroxides is coupled with a depletion in the SiO_2 stishovite content; hence, the faster aggregate velocities characterizing hydrous MORB cannot be reconciled with an increase in the SiO_2 stishovite content.

Typically, slab hydration is associated with a decrease of the slab aggregate velocity as, for example, recently shown for harzburgite and peridotite above and below the 660 km discontinuity (Xu et al., 2020). Our model suggests that the opposite is true for MORB-like lithologies at lower mantle depths. Our model predicts no marked difference in terms of aggregate velocity ratios, v_P/v_S and v_ϕ/v_S, and relative differences of the aggregate velocities between hydrous and anhydrous MORB tend to decrease with pressure.

Based on our data, we evaluated the seismic signature and densities of hydrous MORB in the shallow lower mantle, in a scenario where it is in contact with mantle of pyrolitic composition. Aggregate properties of the pyrolitic mantle were modeled at two different *P-T* conditions, that is, 26 GPa, 1600°C and 28 GPa, 1800°C, corresponding to depths of about 720–760 km (Katsura et al., 2010). Aggregate properties of both hydrous and anhydrous MORB were also calculated at 26 and 28 GPa, but the MORB temperature (T_{MORB}) was varied between 800°C and 1200°C to cover the *T* range expected in slabs in the shallow lower mantle (Kirby et al., 1996). Our model was then used to express the relative differences *d*ln in % between MORB and pyrolite in terms of density ρ and aggregate velocities v_P and v_S (Figure 4). Cold, anhydrous MORB shows the largest difference in terms of density with respect to the pyrolitic mantle—a difference that can reach up to 4.9% if T_{MORB} is assumed to be 800°C. Hydration is expected to decrease MORB density, however, hydrous MORB appears still denser than the pyrolitic mantle at the investigated *P-T* conditions. For example, at 26 GPa and 1200°C T_{MORB}, hydrous MORB is ~1.6% denser than pyrolite at 1600°C (Figure 4).

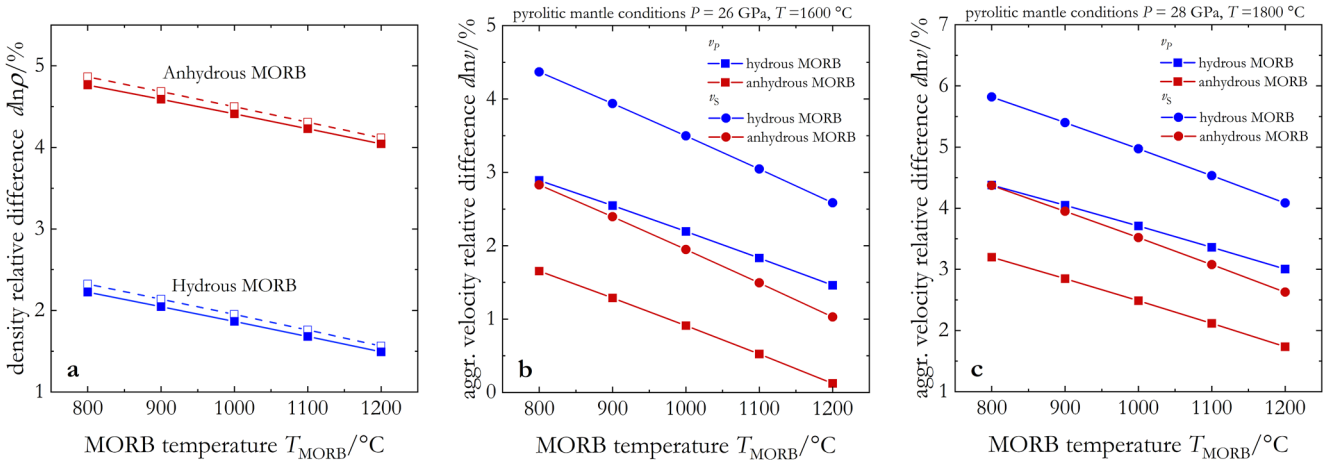

Figure 4. Relative differences in % between MORB and pyrolitic mantle in terms of (a) density as well as (b) and (c) aggregate velocities as function of the MORB temperature (T_{MORB}). Blue and red symbols and lines are used to distinguish between hydrous and anhydrous MORB, respectively. (a) Dashed lines and open symbols: differences between MORB at 26 GPa, and a pyrolitic assemblage at 26 GPa, 1600°C; solid symbols and lines: differences between MORB at 28 GPa, and a pyrolitic assemblage at 28 GPa, 1800°C. (b) Pyrolitic assemblage at 26 GPa, 1600°C; (c) Pyrolitic assemblage at 28 GPa, 1800°C. δ-AlOOH is expected to breakdown between 25 and 30 GPa if T > 1400°C (Piet et al., 2020).

The reduced negative buoyancy of hydrous MORB would make it more likely to stagnate and accumulate in the shallow lower mantle when encountering a viscosity increase at the 660 km discontinuity or in the lower mantle (Deng & Lee, 2017; Marquardt & Miyagi, 2015; Rudolph et al., 2015). Sinking to the deeper mantle may be favored in anhydrous MORB for the opposite reason. At the same time, hydrous MORB produces a significantly stronger seismic contrast with the background mantle, for both shear and compressional velocities (Figure 4), making accumulated hydrous MORB more visible in seismic tomography models. The velocity contrast generally decreases as the MORB in the slab heats up and the P-wave contrast between anhydrous MORB and ambient mantle drops below 1% when their temperature difference is smaller than 600°C (i.e., T_{MORB} > 1000°C) at 26 GPa, suggesting that it may be difficult to detect relatively hot anhydrous MORB in P-wave tomography models (e.g., Fukao & Obayashi, 2013). Hydrous MORB at the same temperature, instead, is still about 2.5% faster as compared to pyrolite and would likely produce a substantially stronger "slab signature" in P-wave tomography models, for example, in the Tonga subduction system (Fukao et al., 2001; van der Hilst, 1995). Since the increase in aggregate velocities is coupled with a density reduction, the seismic contrast between pyrolite and MORB in terms of acoustic impedance, $Z = \rho v$, is not very sensitive to hydration (Figure S9 in Supporting Information S1). This observation is opposite to previous inferences made on the seismic visibility of hydration in the transition zone, where changes in impedance contrast across the 410 km discontinuity were suggested as a characteristic feature of hydration (Buchen et al., 2018).

Data Availability Statement

Acoustic wave velocity data used for c_{ij} determination are available at: https://doi.org/10.6084/m9.figshare.16965124.v1.

Acknowledgments
The authors thank S. Abeykoon for his help with EMP analysis, R. Njul for sample polishing, and F. Trybel for helpful discussions. This study was supported by the IRTG "Deep Earth Volatile Cycles" (GRK 2156/1) and the European Union's Horizon 2020 Research and Innovation Program (ERC Grant 864877). The FEI Scios DualBeam machine at the BGI-Bayreuth was supported by the German Science Foundation (INST 91/315-1 FUGG).

References

Angel, R. J., Alvaro, M., & Gonzalez-Platas, J. (2014). EosFit7c and a Fortran module (library) for equation of state calculations. *Zeitschrift für Kristallographie—Crystalline Materials*, *229*(5), 405–419. https://doi.org/10.1515/zkri-2013-1711

Birch, F. (1947). Finite elastic strain of cubic crystals. *Physical Review*, *71*(11), 809–824. https://doi.org/10.1103/PhysRev.71.809

Buchen, J., Marquardt, H., Speziale, S., Kawazoe, T., Boffa Ballaran, T., & Kurnosov, A. (2018). High-pressure single-crystal elasticity of wadsleyite and the seismic signature of water in the shallow transition zone. *Earth and Planetary Science Letters*, *498*, 77–87. https://doi.org/10.1016/j.epsl.2018.06.027

Cortona, P. (2017). Hydrogen bond symmetrization and elastic constants under pressure of δ-AlOOH. *Journal of Physics: Condensed Matter*, *29*(32), 325505. https://doi.org/10.1088/1361-648X/aa791f

Deng, J., & Lee, K. K. M. (2017). Viscosity jump in the lower mantle inferred from melting curves of ferropericlase. *Nature Communications*, *8*(1), 1997. https://doi.org/10.1038/s41467-017-02263-z

Dewaele, A., Loubeyre, P., & Mezouar, M. (2004). Equations of state of six metals above 94 GPa. *Physical Review B*, *70*(9). 094112. https://doi.org/10.1103/PhysRevB.70.094112

Frost, D. J. (1999). The stability of dense hydrous magnesium silicates in Earth's transition zone and lower mantle. In *Mantle petrology: Field observations and high pressure experimentation: A tribute to Francis R.(Joe) Boyd* (pp. 283–296). The Geochemical Society.

Fukao, Y., & Obayashi, M. (2013). Subducted slabs stagnant above, penetrating through, and trapped below the 660 km discontinuity. *Journal of Geophysical Research: Solid Earth*, *118*(11), 5920–5938. https://doi.org/10.1002/2013JB010466

Fukao, Y., Widiyantoro, S., & Obayashi, M. (2001). Stagnant slabs in the upper and lower mantle transition region. *Reviews of Geophysics*, *39*(3), 291–323. https://doi.org/10.1029/1999RG000068

Garth, T., & Rietbrock, A. (2014). Downdip velocity changes in subducted oceanic crust beneath Northern Japan—Insights from guided waves. *Geophysical Journal International*, *198*(3), 1342–1358. https://doi.org/10.1093/gji/ggu206

Garth, T., & Rietbrock, A. (2017). Constraining the hydration of the subducting Nazca plate beneath Northern Chile using subduction zone guided waves. *Earth and Planetary Science Letters*, *474*, 237–247. https://doi.org/10.1016/j.epsl.2017.06.041

Gleason, A. E., Jeanloz, R., & Kunz, M. (2008). Pressure-temperature stability studies of FeOOH using X-ray diffraction. *American Mineralogist*, *93*(11–12), 1882–1885. https://doi.org/10.2138/am.2008.2942

Gonzalez-Platas, J., Alvaro, M., Nestola, F., & Angel, R. (2016). EosFit7-GUI: A new graphical user interface for equation of state calculations, analyses and teaching. *Journal of Applied Crystallography*, *49*(4), 1377–1382. https://doi.org/10.1107/S1600576716008050

Gréaux, S., Irifune, T., Higo, Y., Tange, Y., Arimoto, T., Liu, Z., & Yamada, A. (2019). Sound velocity of $CaSiO_3$ perovskite suggests the presence of basaltic crust in the Earth's lower mantle. *Nature*, *565*(7738), 218–221. https://doi.org/10.1038/s41586-018-0816-5

Haussühl, S. (2007). *Physical properties of crystals: An introduction*. Wiley-VCH.

Hill, R. S. R. (1952). The elastic behaviour of a crystalline aggregate. *Proceedings of the Physical Society Section B*, *65*, 349. https://doi.org/10.1088/0370-1298/65/5/307

Hsieh, W.-P., Ishii, T., Chao, K.-H., Tsuchiya, J., Deschamps, F., & Ohtani, E. (2020). Spin transition of iron in δ-(Al,Fe)OOH induces thermal anomalies in Earth's lower mantle. *Geophysical Research Letters*, *47*(4), e2020GL087036. https://doi.org/10.1029/2020GL087036

Ikeda, O., Sakamaki, T., Ohashi, T., Goto, M., Higo, Y., & Suzuki, A. (2019). Sound velocity measurements of ε-FeOOH up to 24 GPa. *Journal of Mineralogical and Petrological Sciences*, *114*(3), 155–160. https://doi.org/10.2465/jmps.181115b

Ishii, T., Kojitani, H., & Akaogi, M. (2019). Phase relations of harzburgite and MORB up to the uppermost lower mantle conditions: Precise comparison with pyrolite by multisample cell high-pressure experiments with implication to dynamics of subducted slabs. *Journal of Geophysical Research: Solid Earth*, *124*(4), 3491–3507. https://doi.org/10.1029/2018JB016749

Kantor, I., Prakapenka, V., Kantor, A., Dera, P., Kurnosov, A., Sinogeikin, S., et al. (2012). BX90: A new diamond anvil cell design for X-ray diffraction and optical measurements. *Review of Scientific Instruments*, *83*(12), 125102. https://doi.org/10.1063/1.4768541

Katsura, T., Yoneda, A., Yamazaki, D., Yoshino, T., & Ito, E. (2010). Adiabatic temperature profile in the mantle. *Physics of the Earth and Planetary Interiors*, *183*(1), 212–218. https://doi.org/10.1016/j.pepi.2010.07.001

Kawazoe, T., Ohira, I., Ishii, T., Boffa Ballaran, T., McCammon, C., Suzuki, A., & Ohtani, E. (2017). Single crystal synthesis of δ-(Al,Fe)OOH. *American Mineralogist*, *102*(9), 1953–1956. https://doi.org/10.2138/am-2017-6153

Kirby, S. H., Stein, S., Okal, E. A., & Rubie, D. C. (1996). Metastable mantle phase transformations and deep earthquakes in subducting oceanic lithosphere. *Reviews of Geophysics*, *34*(2), 261–306. https://doi.org/10.1029/96RG01050

Komatsu, K., Kuribayashi, T., Sano, A., Ohtani, E., & Kudoh, Y. (2006). Redetermination of the high-pressure modification of AlOOH from single-crystal synchrotron data. *Acta Crystallographica Section E: Structure Reports Online*, *62*(11), i216–i218. https://doi.org/10.1107/S160053680603916X

Kuribayashi, T., Sano-Furukawa, A., & Nagase, T. (2014). Observation of pressure-induced phase transition of δ-AlOOH by using single-crystal synchrotron X-ray diffraction method. *Physics and Chemistry of Minerals*, *41*(4), 303–312. https://doi.org/10.1007/s00269-013-0649-6

Liu, X., Matsukage, K. N., Nishihara, Y., Suzuki, T., & Takahashi, E. (2019). Stability of the hydrous phases of Al-rich phase D and Al-rich phase H in deep subducted oceanic crust. *American Mineralogist*, *104*(1), 64–72. https://doi.org/10.2138/am-2019-6559

Lu, C., & Chen, C. (2018). High-pressure evolution of crystal bonding structures and properties of FeOOH. *The Journal of Physical Chemistry Letters*, *9*(9), 2181–2185. https://doi.org/10.1021/acs.jpclett.8b00947

Marquardt, H., & Marquardt, K. (2012). Focused ion beam preparation and characterization of single-crystal samples for high-pressure experiments in the diamond-anvil cell. *American Mineralogist*, *97*(2–3), 299–304. https://doi.org/10.2138/am.2012.3911

Marquardt, H., & Miyagi, L. (2015). Slab stagnation in the shallow lower mantle linked to an increase in mantle viscosity. *Nature Geoscience*, *8*(4), 311–314. https://doi.org/10.1038/ngeo2393

Marquardt, H., & Thomson, A. R. (2020). Experimental elasticity of Earth's deep mantle. *Nature Reviews Earth & Environment*, *1*(9), 455–469. https://doi.org/10.1038/s43017-020-0077-3

Mashino, I., Murakami, M., & Ohtani, E. (2016). Sound velocities of δ-AlOOH up to core-mantle boundary pressures with implications for the seismic anomalies in the deep mantle. *Journal of Geophysical Research: Solid Earth*, *121*(2), 595–609. https://doi.org/10.1002/2015JB012477

Nestola, F., Korolev, N., Kopylova, M., Rotiroti, N., Pearson, D. G., Pamato, M. G., et al. (2018). $CaSiO_3$ perovskite in diamond indicates the recycling of oceanic crust into the lower mantle. *Nature*, *555*(7695), 237–241. https://doi.org/10.1038/nature25972

Nishi, M., Irifune, T., Gréaux, S., Tange, Y., & Higo, Y. (2015). Phase transitions of serpentine in the lower mantle. *Physics of the Earth and Planetary Interiors*, *245*, 52–58. https://doi.org/10.1016/j.pepi.2015.05.007

Nishi, M., Tsuchiya, J., Arimoto, T., Kakizawa, S., Kunimoto, T., Tange, Y., et al. (2018). Thermal equation of state of $MgSiO_4H_2$ phase H determined by in situ X-ray diffraction and a multianvil apparatus. *Physics and Chemistry of Minerals*, *45*(10), 995–1001. https://doi.org/10.1007/s00269-018-0980-z

Nishi, M., Tsuchiya, J., Kuwayama, Y., Arimoto, T., Tange, Y., Higo, Y., et al. (2019). Solid solution and compression behavior of hydroxides in the lower mantle. *Journal of Geophysical Research: Solid Earth*, *124*(10), 10231–10239. https://doi.org/10.1029/2019JB018146

Nye, J. F. (1985). *Physical properties of crystals: Their representation by tensors and matrices*. Oxford University Press.

Ohira, I., Jackson, J. M., Solomatova, N. V., Sturhahn, W., Finkelstein, G. J., Kamada, S., et al. (2019). Compressional behavior and spin state of δ-(Al,Fe)OOH at high pressures. *American Mineralogist*, *104*(9), 1273–1284. https://doi.org/10.2138/am-2019-6913

Ohira, I., Ohtani, E., Sakai, T., Miyahara, M., Hirao, N., Ohishi, Y., & Nishijima, M. (2014). Stability of a hydrous δ-phase, AlOOH–$MgSiO_2(OH)_2$, and a mechanism for water transport into the base of lower mantle. *Earth and Planetary Science Letters*, *401*, 12–17. https://doi.org/10.1016/j.epsl.2014.05.059

Ohtani, E. (2020). The role of water in Earth's mantle. *National Science Review*, *7*(1), 224–232. https://doi.org/10.1093/nsr/nwz071

Ohtani, E., Litasov, K., Hosoya, T., Kubo, T., & Kondo, T. (2004). Water transport into the deep mantle and formation of a hydrous transition zone. *Physics of the Earth and Planetary Interiors*, *143–144*, 255–269. https://doi.org/10.1016/j.pepi.2003.09.015

Ohtani, E., Toma, M., Litasov, K., Kubo, T., & Suzuki, A. (2001). Stability of dense hydrous magnesium silicate phases and water storage capacity in the transition zone and lower mantle. *Physics of the Earth and Planetary Interiors*, *124*(1), 105–117. https://doi.org/10.1016/s0031-9201(01)00192-3

Ono, S. (1998). Stability limits of hydrous minerals in sediment and mid-ocean ridge basalt compositions: Implications for water transport in subduction zones. *Journal of Geophysical Research: Solid Earth*, *103*(B8), 18253–18267. https://doi.org/10.1029/98JB01351

Peacock, S. M. (1990). Fluid processes in subduction zones. *Science*, *248*(4953), 329–337. https://doi.org/10.1126/science.248.4953.329

Piet, H., Leinenweber, K. D., Tappan, J., Greenberg, E., Prakapenka, V. B., Buseck, P. R., & Shim, S.-H. (2020). Dehydration of δ-AlOOH in Earth's deep lower mantle. *Minerals*, *10*(4), 384. https://doi.org/10.3390/min10040384

Pillai, S. B., Jha, P. K., Padmalal, A., Maurya, D. M., & Chamyal, L. S. (2018). First principles study of hydrogen bond symmetrization in δ-AlOOH. *Journal of Applied Physics*, *123*(11), 115901. https://doi.org/10.1063/1.5019586

Rudolph, M. L., Lekić, V., & Lithgow-Bertelloni, C. (2015). Viscosity jump in Earth's mid-mantle. *Science*, *350*(6266), 1349–1352. https://doi.org/10.1126/science.aad1929

Sano, A., Ohtani, E., Kubo, T., & Funakoshi, K. (2004). In situ X-ray observation of decomposition of hydrous aluminum silicate $AlSiO_3OH$ and aluminum oxide hydroxide d-AlOOH at high pressure and temperature. *Journal of Physics and Chemistry of Solids*, *65*(8), 1547–1554. https://doi.org/10.1016/j.jpcs.2003.12.015

Sano-Furukawa, A., Hattori, T., Komatsu, K., Kagi, H., Nagai, T., Molaison, J. J., et al. (2018). Direct observation of symmetrization of hydrogen bond in δ-AlOOH under mantle conditions using neutron diffraction. *Scientific Reports*, *8*(1), 1–9. https://doi.org/10.1038/s41598-018-33598-2

Sano-Furukawa, A., Kagi, H., Nagai, T., Nakano, S., Fukura, S., Ushijima, D., et al. (2009). Change in compressibility of δ-AlOOH and δ-AlOOD at high pressure: A study of isotope effect and hydrogen-bond symmetrization. *American Mineralogist*, *94*(8–9), 1255–1261. https://doi.org/10.2138/am.2009.3109

Sano-Furukawa, A., Komatsu, K., Vanpeteghem, C. B., & Ohtani, E. (2008). Neutron diffraction study of δ-AlOOD at high pressure and its implication for symmetrization of the hydrogen bond. *American Mineralogist*, *93*(10), 1558–1567. https://doi.org/10.2138/am.2008.2849

Schulze, K., Buchen, J., Marquardt, K., & Marquardt, H. (2017). Multi-sample loading technique for comparative physical property measurements in the diamond-anvil cell. *High Pressure Research*, *37*(2), 159–169. https://doi.org/10.1080/08957959.2017.1299719

Simonova, D., Bykova, E., Bykov, M., Kawazoe, T., Simonov, A., Dubrovinskaia, N., & Dubrovinsky, L. (2020). Structural Study of δ-AlOOH Up to 29 GPa. *Minerals*, *10*(12), 1055. https://doi.org/10.3390/min10121055

Stixrude, L., & Lithgow-Bertelloni, C. (2005). Thermodynamics of mantle minerals—I. Physical properties. *Geophysical Journal International*, *162*(2), 610–632. https://doi.org/10.1111/j.1365-246X.2005.02642.x

Su, X., Zhao, C., Lv, C., Zhuang, Y., Salke, N., Xu, L., et al. (2020). The effect of iron on the sound velocities of δ-AlOOH up to 135 GPa. *Geoscience Frontiers*, 12, S1674987120302012. https://doi.org/10.1016/j.gsf.2020.08.012

Thompson, E. C., Campbell, A. J., & Tsuchiya, J. (2017). Elasticity of ε-FeOOH: Seismic implications for Earth's lower mantle. *Journal of Geophysical Research: Solid Earth*, *122*(7), 5038–5047. https://doi.org/10.1002/2017JB014168

Thompson, E. C., Davis, A. H., Brauser, N. M., Liu, Z., Prakapenka, V. B., & Campbell, A. J. (2020). Phase transitions in ε-FeOOH at high pressure and ambient temperature. *American Mineralogist*, *105*(12), 1769–1777. https://doi.org/10.2138/am-2020-7468

Trots, D. M., Kurnosov, A., Boffa Ballaran, T., Tkachev, S., Zhuravlev, K., Prakapenka, V., et al. (2013). The Sm:YAG primary fluorescence pressure scale. *Journal of Geophysical Research: Solid Earth*, *118*(11), 5805–5813. https://doi.org/10.1002/2013JB010519

Trots, D. M., Kurnosov, A., Vasylechko, L., Berkowski, M., Boffa Ballaran, T., & Frost, D. J. (2011). Elasticity and equation of state of $Li_2B_4O_7$. *Physics and Chemistry of Minerals*, *38*(7), 561–567. https://doi.org/10.1007/s00269-011-0428-1

Tsuchiya, J., & Tsuchiya, T. (2009). Elastic properties of δ-AlOOH under pressure: First principles investigation. *Physics of the Earth and Planetary Interiors*, *174*(1–4), 122–127. https://doi.org/10.1016/j.pepi.2009.01.008

van der Hilst, R. (1995). Complex morphology of subducted lithosphere in the mantle beneath the Tonga trench. *Nature*, *374*(6518), 154–157. https://doi.org/10.1038/374154a0

Wang, W., Xu, Y., Sun, D., Ni, S., Wentzcovitch, R., & Wu, Z. (2020). Velocity and density characteristics of subducted oceanic crust and the origin of lower-mantle heterogeneities. *Nature Communications*, *11*(1), 64. https://doi.org/10.1038/s41467-019-13720-2

Xu, C., Gréaux, S., Inoue, T., Noda, M., Sun, W., Kuwahara, H., & Higo, Y. (2020). Sound Velocities of Al-Bearing Phase D up to 22 GPa and 1300 K. *Geophysical Research Letters*, *47*(18). https://doi.org/10.1029/2020GL088877

Xu, C., Nishi, M., & Inoue, T. (2019). Solubility behavior of δ-AlOOH and ε-FeOOH at high pressures. *American Mineralogist*, *104*(10), 1416–1420. https://doi.org/10.2138/am-2019-7064

References From the Supporting Information

Angel, R. J., & Finger, L. W. (2011). SINGLE: A program to control single-crystal diffractometers. *Journal of Applied Crystallography*, *44*(1), 247–251. https://doi.org/10.1107/S0021889810042305

Boehler, R., & De Hantsetters, K. (2004). New anvil designs in diamond-cells. *High Pressure Research*, *24*(3), 391–396. https://doi.org/10.1080/08957950412331323924

Buchen, J. (2018). *The elastic properties of Wadsleyite and Stishovite at high pressures: Tracing deep Earth material cycles*. University of Bayreuth. https://doi.org/10.15495/EPub_UBT_00004410

Chantel, J., Frost, D. J., McCammon, C. A., Jing, Z., & Wang, Y. (2012). Acoustic velocities of pure and iron-bearing magnesium silicate perovskite measured to 25 GPa and 1200 K. *Geophysical Research Letters*, *39*(19). https://doi.org/10.1029/2012GL053075

Cottaar, S., Heister, T., Rose, I., & Unterborn, C. (2014). BurnMan: A lower mantle mineral physics toolkit. *Geochemistry, Geophysics, Geosystems*, *15*(4), 1164–1179. https://doi.org/10.1002/2013GC005122

Criniti, G., Kurnosov, A., Ballaran, T. B., & Frost, D. J. (2021). Single-crystal elasticity of $MgSiO_3$ bridgmanite to mid-lower mantle pressure. *Journal of Geophysical Research: Solid Earth*, *126*(5). e2020JB020967. https://doi.org/10.1029/2020JB020967

Duan, Y., Sun, N., Wang, S., Li, X., Guo, X., Ni, H., et al. (2018). Phase stability and thermal equation of state of δ-AlOOH: Implication for water transportation to the Deep Lower Mantle. *Earth and Planetary Science Letters*, *494*, 92–98. https://doi.org/10.1016/j.epsl.2018.05.003

Fischer, R. A., Campbell, A. J., Shofner, G. A., Lord, O. T., Dera, P., & Prakapenka, V. B. (2011). Equation of state and phase diagram of FeO. *Earth and Planetary Science Letters*, *304*(3), 496–502. https://doi.org/10.1016/j.epsl.2011.02.025

Gréaux, S., Kono, Y., Wang, Y., Yamada, A., Zhou, C., Jing, Z., et al. (2016). Sound velocities of aluminum-bearing stishovite in the mantle transition zone. *Geophysical Research Letters*, *43*(9), 4239–4246. https://doi.org/10.1002/2016GL068377

Ishii, T., Kojitani, H., & Akaogi, M. (2011). Post-spinel transitions in pyrolite and Mg_2SiO_4 and akimotoite-perovskite transition in $MgSiO_3$: Precise comparison by high-pressure high-temperature experiments with multi-sample cell technique. *Earth and Planetary Science Letters*, *309*(3), 185–197. https://doi.org/10.1016/j.epsl.2011.06.023

Klotz, S., Chervin, J.-C., Munsch, P., & Marchand, G. L. (2009). Hydrostatic limits of 11 pressure transmitting media. *Journal of Physics D: Applied Physics*, *42*(7), 075413. https://doi.org/10.1088/0022-3727/42/7/075413

Kono, Y., Irifune, T., Higo, Y., Inoue, T., & Barnhoorn, A. (2010). P-V-T relation of MgO derived by simultaneous elastic wave velocity and in situ X-ray measurements: A new pressure scale for the mantle transition region. *Physics of the Earth and Planetary Interiors*, *183*(1), 196–211. https://doi.org/10.1016/j.pepi.2010.03.010

Kurnosov, A., Kantor, I., Boffa-Ballaran, T., Lindhardt, S., Dubrovinsky, L., Kuznetsov, A., & Zehnder, B. H. (2008). A novel gas-loading system for mechanically closing of various types of diamond anvil cells. *Review of Scientific Instruments*, *79*(4), 045110. https://doi.org/10.1063/1.2902506

Kurnosov, A., Marquardt, H., Frost, D. J., Ballaran, T. B., & Ziberna, L. (2017). Evidence for a Fe^{3+}-rich pyrolitic lower mantle from (Al,Fe)-bearing bridgmanite elasticity data. *Nature*, *543*(7646), 543–546. https://doi.org/10.1038/nature21390

Lindsay, S. M., Anderson, M. W., & Sandercock, J. R. (1981). Construction and alignment of a high performance multipass vernier tandem Fabry-Perot interferometer. *Review of Scientific Instruments*, *52*(10), 1478–1486. https://doi.org/10.1063/1.1136479

Litasov, K. D., & Ohtani, E. (2005). Phase relations in hydrous MORB at 18–28GPa: Implications for heterogeneity of the lower mantle. *Physics of the Earth and Planetary Interiors*, *150*(4), 239–263. https://doi.org/10.1016/j.pepi.2004.10.010

McCammon, C. A. (1994). A Mössbauer milliprobe: Practical considerations. *Hyperfine Interactions*, *92*(1), 1235–1239. https://doi.org/10.1007/BF02065761

Pamato, M. G. (2014). *Single-crystal elasticity of Al-rich phases in the Earth's transition zone and lower mantle (Doctoral thesis)*. Retrieved from https://epub.uni-bayreuth.de/2082/

Poirier, J.-P. (2000). Lattice vibrations. In *Introduction to the physics of the Earth's interior* (2nd ed., pp. 27–62). Cambridge University Press. https://doi.org/10.1017/CBO9781139164467.006

Prescher, C., McCammon, C., & Dubrovinsky, L. (2012). *MossA*: A program for analyzing energy-domain Mössbauer spectra from conventional and synchrotron sources. *Journal of Applied Crystallography*, *45*(2), 329–331. https://doi.org/10.1107/S0021889812004979

Speziale, S., Marquardt, H., & Duffy, T. S. (2014). Brillouin scattering and its application in geosciences. *Reviews in Mineralogy and Geochemistry*, *78*(1), 543–603. https://doi.org/10.2138/rmg.2014.78.14

Stixrude, L., & Lithgow-Bertelloni, C. (2011). Thermodynamics of mantle minerals—II. Phase equilibria. *Geophysical Journal International*, *184*(3), 1180–1213. https://doi.org/10.1111/j.1365-246X.2010.04890.x

Tange, Y., Takahashi, E., Nishihara, Y., Funakoshi, K., & Sata, N. (2009). Phase relations in the system MgO-FeO-SiO2 to 50 GPa and 2000°C: An application of experimental techniques using multianvil apparatus with sintered diamond anvils. *Journal of Geophysical Research: Solid Earth*, *114*(B2). https://doi.org/10.1029/2008JB005891

Whitfield, C. H., Brody, E. M., & Bassett, W. A. (1976). Elastic moduli of NaCl by Brillouin scattering at high pressure in a diamond anvil cell. *Review of Scientific Instruments*, *47*(8), 942–947. https://doi.org/10.1063/1.1134778

Xu, W., Lithgow-Bertelloni, C., Stixrude, L., & Ritsema, J. (2008). The effect of bulk composition and temperature on mantle seismic structure. *Earth and Planetary Science Letters*, *275*(1), 70–79. https://doi.org/10.1016/j.epsl.2008.08.012

Zha, C.-S., Mao, H., Hemley, R. J., & Duffy, T. S. (1998). Recent progress in high-pressure Brillouin scattering: Olivine and ice. *The Review of High Pressure Science and Technology*, *7*, 739–741. https://doi.org/10.4131/jshpreview.7.739